

Qubit-assisted quantum metrology

Peng Chen¹ and Jun Jing^{1,*}

¹*School of Physics, Zhejiang University, Hangzhou 310027, Zhejiang, China*

We propose a quantum metrology protocol based on a two-step joint evolution of the probe system and an ancillary qubit and a single-shot projective measurement. With an optimized initialization of the ancillary qubit, the quantum Fisher information (QFI) about the phase parameter encoded in the probe system is found to be determined by the expectation value of the square of a time-optimized phase generator, independent of the probe state. Therefore, QFI can approach the Heisenberg scaling N^2 with respect to the quantum number N , even when the probe system is prepared in a classical state. We find that this scaling behavior is robust against the imperfections in preparing the ancillary qubit and controlling the evolution time. Using the time-reversal strategy, the classical Fisher information (CFI) in our metrology protocol is saturated with its quantum counterpart. Our work thus paves an economical way to realize the Heisenberg-scaling limit in metrology precision with no use of entanglement or squeezing.

I. INTRODUCTION

Quantum metrology aims to use various quantum resources including entanglement and squeezing to exceed the standard quantum limit (SQL), where the uncertainty decreases with $1/\sqrt{N}$, on performing measurements of physical parameters [1–5]. Examples of these parameters are the phases of evolving quantum systems encoded in multiple applications [6–8], such as gravitational wave detection [9], biological sensing [10, 11], atomic clocks [12, 13], and magnetometry [14]. A conventional protocol for precision metrology reaching the Heisenberg limit (HL) [15–18], where the uncertainty decreases with $1/N$, consists of a well-prepared probe system (in e.g., the NOON state), a definite unitary transformation to encode the phase parameter θ into the probe state, a practical measurement, and a suitable data processing to produce an estimator $\tilde{\theta}(x)$ about the parameter θ from the outcome x . The estimation precision is quantified by the standard deviation $\delta\theta = \langle [\tilde{\theta}(x) - \theta]^2 \rangle^{1/2}$, which is under the constraint of the Cramér-Rao inequality [7, 19]: $\delta\theta \geq 1/\sqrt{F_c}$ with F_c the classical Fisher information (CFI). Maximizing F_c over all possible measurements gives rise to the quantum Fisher information (QFI) F_Q and hence the quantum Cramér-Rao bound $\delta\theta_{\min} = 1/\sqrt{F_Q}$ [20–24] on the attainable sensitivity to estimate θ .

The optimal precision $\delta\theta_{\min}$ generally improves with an increasing quantum number N of the probe state employed in the measurement. With the probe system in separable states, we have $F_Q \sim N$ for the standard quantum limit. With particular entangled probe states, such as the NOON state, we have the so-called Heisenberg scaling $F_Q \sim N^2$ and hence the metrological precision attains HL [25–28]. However, the difficulty in obtaining NOON states with a large N hinders its practical applications [29–32]. An alternative method to improve the precision is to use the squeezed spin state [33–36], that

is typically generated by the one-axis twisting (OAT) and two-axis twisting (TAT) interactions [37, 38]. The collective OAT interaction $H_{\text{OAT}} \propto J_z^2$ gives rise to a squeezing degree $\propto 1/N^{2/3}$ for N particles, which has been implemented in Bose-Einstein condensation (BEC) systems [39, 40], trapped ions [41, 42], superconducting qubits [43, 44], and warm vapors in glass cells [45–47]. Under the TAT interaction $H_{\text{TAT}} \propto J_x^2 + J_y^2$, that is mainly reported in theoretical schemes [38, 48], the squeezing degree $\propto 1/N$ approaches HL. It remains however a challenge in practice since the interaction Hamiltonian is rarely found in current platforms [48–50]. In quantum optics, the archetype of a metrology experiment for phase estimation is the Mach-Zehnder interferometer. When the beam splitters are replaced with optical parametric amplifiers, the resulting $SU(1, 1)$ interferometer can reach HL only by inputting coherent states [8, 51–55]. However, its sensitivity to the internal losses eventually makes it work even below SQL [56].

Recently, the coupling with an ancillary system is found to outperform SQL in the estimation precision about the phase parameter. In a protocol for measuring the light rotation with indefinite time direction [57], an ancillary system serves as a quantum switch leading to a superposition of opposite rotations of the probe system. The rotation precision can thus be enhanced to HL even by using classical probe states. And a precision of 12.9 nrad on light rotation measurement has been experimentally realized with a 150-order Laguerre-Gaussian beam. Motivated by the time reversal strategy [8, 58, 59], based on which a quantum metrology protocol can approach the Cramér-Rao bound for certain parameters, Ref. [60] proposed a controlled protocol based on a two-photonic-mode system and an ancillary qubit. In this protocol, the interaction between the photonic system and the qubit can be manipulated by the external control fields to implement the unitary transformations along the forward- and reverse-time directions. The forward-time evolution generates a photonic entangled NOON state to improve QFI and the reverse-time evolution allows CFI to saturate with its quantum counterpart.

In this work, we present a qubit-assisted metrology

* Email address: jingjun@zju.edu.cn

protocol to estimate the phase parameter θ encoded into the probe system (a spin ensemble) during a time evolution, which is based on the time-reversal strategy and a projective measurement. With a properly prepared ancillary qubit, QFI can be modified from the variance of the phase generator to the mean square of that with respect to the probe state. In this case, QFI can be enhanced up to the Heisenberg scaling in terms of the total spin number ($F_Q \propto N^2$) even when the probe spin ensemble is prepared as a classical state. The scaling behavior is robust against the imperfections about the initial state of the ancillary qubit and the optimized evolution time of the whole system. Moreover, CFI of our protocol is found to be coincident with QFI by the time-reversal strategy.

The rest of this work is structured as follows. In Sec. II, we describe the circuit model of our metrology protocol with the ancillary qubit. In Sec. III, we investigate the conditions for the time-reversal strategy. A detailed derivation about the relevant evolution operator is provided in Appendix A. In Sec. IV, we find that QFI in our protocol can be expressed as the mean square of an optimized phase generator with respect to the probe initial state. That underlies the Heisenberg-limited sensitivity for a large N even when the probe is in the mixed state. In Sec. V, we calculate CFI in our protocol as the extractable information from the probability distribution of the output state upon the projective measurement. In Sec. VI, we adapt our protocol to an alternative interaction between the probe system and an ancillary qubit. We summarize our work in Sec. VII.

II. HAMILTONIAN AND METROLOGY MODEL

Consider a model consisting of a spin ensemble as a measurement probe and an ancillary spin-1/2. The full Hamiltonian including the free Hamiltonian H_0 and interaction part H_I reads ($\hbar \equiv 1$)

$$H = H_0 + H_I = \omega_P J_z + \omega_A \sigma_z + g J_z \sigma_z, \quad (1)$$

where $J_\alpha = \sum_{k=1}^N \sigma_\alpha^k / 2$, $\alpha = x, y, z$, denotes the collective spin operator with σ_α^k the Pauli matrix of the k th probe spin, ω_P and ω_A represent the energy splitting of the probe spin and the ancillary spin, respectively, and g is the coupling strength between the two components.

The full Hamiltonian (1) is feasible in various experiments. In quantum dots [61], J_z and σ_z describe the nuclear spins and the electron spin, respectively. In BEC, the Hamiltonian can be realized by two cavities containing two-component BECs coupled by an optical fiber [62], where the operators J_z and σ_z correspond to the Schwinger boson operators $a^\dagger a - b^\dagger b$ with a^\dagger and b^\dagger being bosonic creation operators for two orthogonal quantum states. Also, our interaction Hamiltonian is similar to that by coupling an atomic ensemble to a light beam with the off-resonant Faraday interaction [46, 47], where J_z is the sum of the total angular momentum of

individual atoms and σ_z denotes the Stokes operator associated with the distinction between the number operators of the photons polarized along orthogonal bases.

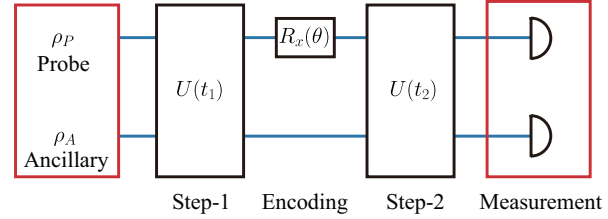


FIG. 1. Circuit model of our qubit-assisted metrology consisting of a two-step evolution interrupted by the parametric encoding and a single-shot measurement. Step 1 and 2 denote the free joint unitary evolution $U(t_1)$ and its time reversal $U(t_2)$, respectively, in between which a to-be-estimated parameter θ is encoded into the probe state via a unitary operation $R_x(\theta)$. The output state is determined by a projective measurement on either the full system or the ancillary qubit.

The probe spin ensemble and the ancillary qubit are initially separable, i.e., the input state of the full system is a product state $\rho_P \otimes \rho_A$. The whole circuit in Fig. 1 can be described by

$$U_\theta = U(t_2) R_x(\theta) U(t_1) = e^{-iHt_2} e^{-i\theta J_x} e^{-iHt_1}, \quad (2)$$

where the two steps of evolution last t_1 and t_2 , respectively. During Step 1, the probe and ancillary system are entangled. Through the parametric encoding of a negligible evolution time, we obtain a phase parameter θ by a spin rotation $R_x(\theta) = \exp(-i\theta J_x)$ of the probe system. Experimentally θ can be accumulated during the precessing about z -axis [39, 63, 64] induced by a certain interaction between the probe and a to-be-measured system. Then the rotation about x -axis could be performed by a sequence of $R_x(\theta) = R_y(\pi/2) R_z(\theta) R_y(-\pi/2)$, where $R_y(\pm\pi/2)$ indicates a $\pi/2$ pulse about y -axis. The duration time of Step 2 is determined by t_1 under the time-reversal strategy [8, 58, 59]. On the last stage of the circuit, a projective measurement about the full system is performed on the output state $\rho(\theta) \equiv U_\theta \rho_P \otimes \rho_A U_\theta^\dagger$, whose success probability can be used to infer the Fisher information about the estimated parameter. When the input state of the probe (spin ensemble) is an eigenstate of U_θ , the maximum parameter information can be obtained only by performing a projective measurement on the ancillary qubit.

It has been shown [8, 58, 59] that the measurement precision can be certainly enhanced such that CFI is increased to be equivalent to QFI when the joint evolution operator $U(t_2)$ becomes the time reversal of $U(t_1)$, i.e.,

$$U(t_2) = U^\dagger(t_1). \quad (3)$$

It indicated that the full system traces back its entanglement generation trajectory and returns to the input state if no phase is encoded.

III. CONDITIONS FOR TIME REVERSAL

According to the definition of U_θ in Eq. (2) and the requirement for time reversal in Eq. (3), it is evident that

$$\begin{aligned} U_{\theta=0} &= e^{-iH(t_1+t_2)} = U(t_1+t_2) = \mathcal{I}^{2(N+1)} \\ &= \sum_{m=-j}^j |j, m\rangle\langle j, m| \otimes (|e\rangle\langle e| + |g\rangle\langle g|), \end{aligned} \quad (4)$$

where $N = 2j$ is the total spin number of the probe ensemble, \mathcal{I}^n is the identity matrix with dimension n , $|j, m\rangle$ is the eigenstate of the operators J_z with eigenvalue m , and $|g\rangle$ and $|e\rangle$ denote the ground and excited states of the ancillary spin, respectively. Using the full Hamiltonian (1), we have

$$\begin{aligned} U(t_1+t_2) &= U(T) = \sum_{m=-j}^j |j, m\rangle\langle j, m| \\ &\otimes (C_{e,m}|e\rangle\langle e| + C_{g,m}|g\rangle\langle g|), \end{aligned} \quad (5)$$

where $C_{e,m} = \exp\{-i[\omega_A + m(\omega_P + g)]T\}$ and $C_{g,m} = \exp\{i[\omega_A - m(\omega_P - g)]T\}$ with $T \equiv t_1 + t_2$. It is found that when

$$C_{e,m} = C_{g,m'}, \quad (6)$$

Eq. (4) becomes equivalent to Eq. (5) up to a global phase. Given the expression in Eq. (6), we have

$$(e^{igT})^{m+m'} (e^{i\omega_P T})^{m-m'} = e^{-2i\omega_A T}. \quad (7)$$

The parity of the probe-spin number N determines whether the eigenvalue m is an integer or a half-integer. When N is even, m is an integer and then $m \pm m'$ are the same in parity. A sufficient solution for Eq. (7) is thus $e^{igT} = e^{i\omega_P T} = \pm 1$. Straightforwardly we have

$$\frac{gT}{\pi} = n_1, \quad \frac{\omega_P T}{\pi} = n_1 + 2n_2, \quad \frac{\omega_A T}{\pi} = n_3, \quad (8)$$

where n_j 's, $j = 1, 2, 3$, are proper integers subject to the given magnitudes of g , ω_P , and ω_A . When N is odd, $m \pm m'$ are different in parity. The solution can thus be written as

$$\frac{gT}{\pi} = n_1, \quad \frac{\omega_P T}{\pi} = n_1 + 2n_2, \quad \frac{\omega_A T}{\pi} = \frac{n_1}{2} + n_4, \quad (9)$$

where n_j 's, $j = 1, 2, 4$, are proper integers. For either even or odd, it might be hard to find the exact solution of T if g , ω_P , and ω_A are incommensurable.

The analytical results about T can be confirmed by the numerical simulation over the normalized trace of the unitary operator $U(T)$,

$$\mathcal{F}(T) = \frac{|\text{Tr}[U(T)]|}{2(N+1)}. \quad (10)$$

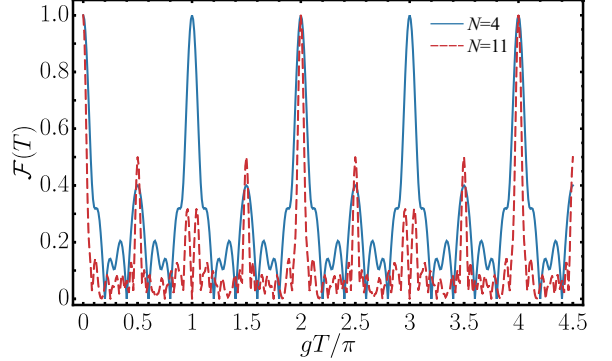


FIG. 2. Normalized trace $\mathcal{F}(T)$ as a function of the full evolution time T with various spin number N . $\omega_P = \omega_A = 3g$.

When $\mathcal{F}(T) = 1$, we have $U(T) = \mathcal{I}^{2(N+1)}$ up to a global phase and vice versa. Once T is specified by a unit trace, the time-reversal condition in Eq. (3) is automatically satisfied by setting $t_2 = T - t_1$.

In Fig. 2, we demonstrate the normalized trace $\mathcal{F}(T)$ as a function of the evolution time T exemplified with $N = 4$ and $N = 11$ under a fixed setting that $\omega_P = \omega_A = 3g$. The parity of the probe-spin number N determines the time when the normalized trace $\mathcal{F}(T)$ attains unit. When $N = 4$ (the even case, see the blue solid line), it is found that the normalized trace attains the maximum value when the full evolution time T is a multiple of π/g . For example, when $T = \pi/g$, Eq. (8) is valid for $n_1 = 1$, $n_2 = 1$, and $n_3 = 3$. When $N = 11$ (the odd case, see the red dashed line), the normalized trace attains unit when T is a multiple of $2\pi/g$. Particularly, $T = 2\pi/g$ is attained by setting $n_1 = 2$, $n_2 = 2$, and $n_4 = 5$ in Eq. (9). Moreover in case of an odd N , one can find that the unitary operator becomes

$$U(T) = \mathcal{I}^{N+1} \otimes \sigma_z \quad (11)$$

up to a global phase when T is an odd multiple of π/g . It will give rise to a vanishing normalized trace $\mathcal{F}(T) = 0$. And then the time-reversal strategy is broken. Therefore, choosing a probe ensemble with an even number of spins can significantly accelerate our metrology protocol.

IV. QUANTUM FISHER INFORMATION

Suppose that we have found an exact solution about T on demand of the time-reversal strategy, then the whole unitary evolution operator in Eq. (2) can be rewritten as

$$U_\theta = e^{iHt_1} e^{-i\theta J_x} e^{-iHt_1}. \quad (12)$$

Using the Baker-Campbell-Hausdorff formula, we have (the details are provided in Appendix A)

$$U_\theta = e^{-i\theta [\cos(gt_1)J(-\phi) - \sin(gt_1)J(\frac{\pi}{2} - \phi)\sigma_z]}, \quad (13)$$

where the phase generator forms as $J(\phi) \equiv \cos(\phi)J_x + \sin(\phi)J_y$ with $\phi = \omega_P t_1$. We are now on the stage of analyzing the precision limit of the qubit-assisted metrology.

Initially, the ancillary qubit is assumed to be a pure qubit $\rho_A = |\varphi\rangle\langle\varphi|$ with [34, 65]

$$|\varphi\rangle = \cos\left(\frac{\theta_0}{2}\right)|e\rangle + e^{-i\phi_0}\sin\left(\frac{\theta_0}{2}\right)|g\rangle. \quad (14)$$

Here θ_0 and ϕ_0 determine the population imbalance and the relative phase between the two bases, respectively. Without loss of generality, we set the azimuthal angle $\phi_0 = 0$. For the input state of the probe system, always it can be written as

$$\rho_P = \sum_{i=1}^d p_i |\psi_i\rangle\langle\psi_i| \quad (15)$$

in spectral decomposition, where d is the dimension of the density matrix, p_i 's are the eigenvalues, and $|\psi_i\rangle$'s are the corresponding eigenstates.

Using Eqs. (14) and (15), QFI of the output state associated with the metrology precision for estimating θ is given by [20, 21, 32, 66]

$$F_Q = \sum_{i=1}^d 4p_i \langle\psi_i|\langle\varphi|(\partial_\theta U_\theta)^\dagger(\partial_\theta U_\theta)|\varphi\rangle|\psi_i\rangle - \sum_{i,j=1}^d \frac{8p_i p_j}{p_i + p_j} |\langle\psi_i|\langle\varphi|U_\theta^\dagger(\partial_\theta U_\theta)|\varphi\rangle|\psi_j\rangle|^2 \quad (16)$$

with $p_i \neq 0$. We actually obtain a difference between a positive expression, that is vital to achieve Heisenberg scaling as shown in the following, and a non-positive one. A straightforward method to enhance QFI is thus to minimize the magnitude of the second term in Eq. (16) or more generally and precisely to minimize the expression inside the absolute value. Using Eq. (13), we have

$$\langle\psi_i|\langle\varphi|U_\theta^\dagger(\partial_\theta U_\theta)|\varphi\rangle|\psi_i\rangle = \cos(gt_1)\langle J(-\phi)\rangle_{\psi_i} - \sin(gt_1)\langle\sigma_z\rangle_\varphi \left\langle J\left(\frac{\pi}{2} - \phi\right)\right\rangle_{\psi_i}, \quad (17)$$

where $\langle A \rangle_\psi \equiv \langle\psi|A|\psi\rangle$. Under a proper state of the ancillary qubit and an optimized evolution time for Step 1, i.e.,

$$\theta_0^{\text{opt}} = \frac{\pi}{2}, \quad t_{1,\text{opt}} = \left(n + \frac{1}{2}\right) \frac{\pi}{g}, \quad (18)$$

with an integer n , the two terms in Eq. (17) can vanish at the same time for arbitrary probe state ψ_i . Consequently, Eq. (13) becomes $U_\theta = \exp[i\theta J(\pi/2 - \phi_{\text{opt}})\sigma_z]$ with $\phi_{\text{opt}} \equiv \omega_P t_{1,\text{opt}}$.

We emphasize that Eq. (17) presents the main advantage of our qubit-assisted metrology over a conventional parameter estimation [15–18]. For a conventional metrology, in which only the probe state is considered, Eq. (17)

becomes

$$\langle\psi_i|U_\theta^\dagger(\partial_\theta U_\theta)|\psi_i\rangle = \langle\cos(\omega_P t_1)J_x - \sin(\omega_P t_1)J_y\rangle_{\psi_i}. \quad (19)$$

Hardly one can find a state-independent time t_1 leading to $\langle\psi_i|U_\theta^\dagger(\partial_\theta U_\theta)|\psi_i\rangle = 0$, since $\cos(\omega_P t_1)$ and $\sin(\omega_P t_1)$ cannot simultaneously become zero.

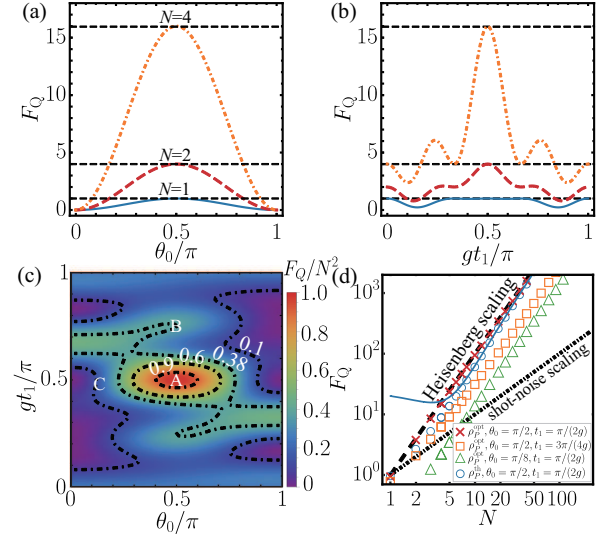


FIG. 3. (a) QFI as a function of θ_0 with a fixed $t_1 = \pi/(2g)$ and various probe-spin number N , (b) QFI as a function of the renormalized evolution time gt_1 with a fixed $\theta_0 = \pi/2$ and various N , (c) Renormalized QFI F_Q/N^2 in space of θ_0 and gt_1 with $N = 4$, and (d) QFI as a function of N for $\rho_P = \rho_P^{\text{opt}} = |j, j\rangle_{\text{opt}}\langle j, j|$, $\theta_0 = \pi/2$, and $t_1 = \pi/(2g)$ (red crosses); for ρ_P^{opt} , $\theta_0 = \pi/2$, and $t_1 = 3\pi/(4g)$ (orange squares); for ρ_P^{opt} , $\theta_0 = \pi/8$, and $t_1 = \pi/(2g)$ (green triangles); for ρ_P^{th} with $\beta = 1$, $\theta_0 = \pi/2$, and $t_1 = \pi/(2g)$ [blue circles for numerical results and blue solid line for analytical expression in Eq. (23)]. In (a), (b), (c), and (d), the black dashed line and the black dot-dashed line indicate the Heisenberg scaling N^2 and the shot-noise scaling N , respectively. $\omega_P = \omega_A = 3g$

By Eqs. (16) and (18), QFI becomes the mean square of a phase generator with respect to the probe state, i.e.,

$$F_Q = 4 \sum_{i=1}^d p_i \left\langle J\left(\frac{\pi}{2} - \phi_{\text{opt}}\right)^2 \right\rangle_{\psi_i}, \quad (20)$$

which is a weighted average over the expectation value for the operator $J(\pi/2 - \phi_{\text{opt}})^2$ within each eigenstate $\{|\psi_i\rangle\}$ of ρ_P . Straightforwardly, QFI can attain its peak value $F_Q = N^2$ when the probe spin ensemble is prepared in a pure state $|j, j\rangle_{\text{opt}}$, or $|j, -j\rangle_{\text{opt}}$, and or a mixed state over them, such as $\rho_P = (|j, j\rangle_{\text{opt}}\langle j, j| + |j, -j\rangle_{\text{opt}}\langle j, -j|)/2$, where $|j, m\rangle_{\text{opt}}$ with $-j \leq m \leq j$ denotes the eigenstate for the optimized collective angular momentum operator $J(\pi/2 - \phi_{\text{opt}})$. Subjected to the duration time $t_{1,\text{opt}}$ and the time-reversal strategy, the bases $|j, m\rangle_{\text{opt}}$'s are determined by the magnitudes of g , ω_P , and ω_A . Heisenberg scaling can therefore be approached under optimized θ_0 and t_1 .

This condition could be confirmed by the numerical simulation in Fig. 3, where the input state of the probe ensemble is set as $\rho_P^{\text{opt}} = |j, j\rangle_{\text{opt}}\langle j, j|$ and the frequencies of both probe spin and ancillary qubit are the same as in Fig. 2. Figure 3(a) describes the dependence of the quantum Fisher information F_Q on the input parameter of the ancillary qubit θ_0 under an optimized evolution time $t_{1,\text{opt}}$ given by Eq. (18). It is shown that F_Q follows the Heisenberg scaling when $\theta_0 = \pi/2$ for various N . In Fig. 3(b), the initial state of the ancillary qubit is fixed with $\theta_0 = \pi/2$ and F_Q finds its peak at $t_1 = \pi/(2g)$ as expected by Eq. (18). In both Fig. 3(a) and Fig. 3(b), F_Q is symmetrical to the optimized points and varies smoothly around them, indicating that our metrology protocol is not sensitive to the imperfections in parametric control.

In Fig. 3(c), we take $N = 4$ and demonstrate the renormalized QFI F_Q/N^2 in the space of θ_0 and t_1 . The black dot-dashed lines are the contour lines indicating the proportional coefficients. The central region around point-A describes the most optimized condition that is in agreement with Eq. (18). The surrounding regions about point-B and point-C describe less optimized conditions with t_1 or θ_0 largely departing from Eq. (18). The behaviors for these points with various N are plotted with the red crosses, the orange squares, and the green triangles, respectively, in Fig. 3(d). The first one sticks to its upper bound $F_Q = N^2$, and the last two are apparently below this bound. However, a similar behavior to Heisenberg scaling $F_Q \propto N^2$ can be restored when N is sufficiently large, although θ_0 or gt_1 is not optimized.

It is interesting to find that QFI could approach Heisenberg scaling even if the probe ensemble is prepared as a thermal state in the bases of $|j, m\rangle_{\text{opt}}$, i.e.,

$$\rho_P^{\text{th}} = \frac{1}{Z_\beta} e^{-\beta J(\pi/2 - \phi_{\text{opt}})}, \quad (21)$$

where $Z_\beta = \text{Tr}\{\exp[-\beta J(\pi/2 - \phi_{\text{opt}})]\}$ is the partition function and β is the inverse temperature. By Eqs. (20) and (21), we have

$$\begin{aligned} F_Q &= 4 \frac{\sum_{m=-N/2}^{N/2} m^2 \exp(-m\beta)}{\sum_{m=-N/2}^{N/2} \exp(-m\beta)} \\ &= \frac{1}{(e^\beta - 1)^2} \left[N^2 \frac{1 - e^{(3+N)\beta}}{1 - e^{(1+N)\beta}} \right. \\ &\quad + (N+2)^2 \frac{e^{2\beta} - e^{(1+N)\beta}}{1 - e^{(1+N)\beta}} \\ &\quad \left. + (N^2 + 2N - 2) \frac{2e^{(2+N)\beta} - 2e^\beta}{1 - e^{(1+N)\beta}} \right]. \end{aligned} \quad (22)$$

And then for a large probe-spin number, i.e., $N \gg 1$, it is approximated as

$$\begin{aligned} F_Q &\approx \frac{e^{2\beta} N^2 + (N+2)^2 - 2e^\beta (N^2 + 2N - 2)}{(e^\beta - 1)^2} \\ &= N^2 - \frac{4}{e^\beta - 1} N + 4 \frac{e^\beta + 1}{(e^\beta - 1)^2}. \end{aligned} \quad (23)$$

Clearly $F_Q = N^2$ when $\beta \rightarrow \infty$. It is indicated that the Heisenberg-scaling behavior N^2 dominates QFI at least in the low-temperature limit. And F_Q will become divergent in the high-temperature limit, i.e., $\beta \rightarrow 0$, which cannot be used to estimate the metrology precision. In Fig. 3(d), the analytical expression in Eq. (23) is confirmed to match the numerical result and both of them approach the Heisenberg scaling, provided $N \gg 1$.

V. CLASSICAL FISHER INFORMATION

In a practical scenario of parametric estimation, CFI is defined by catching the amount of information encoded in the probability distribution for the output state under the estimation process [67–69]. And it is upper bounded by its quantum counterpart on the metrology precision. With the time-reversal strategy, it was shown [8, 58, 59] that CFI can be saturated with QFI, which indicates that all the information encoded in the probe state from the output probability distribution has been extracted. We now derive CFI of our protocol under the same optimized settings in Eq. (18) with $n = 0$ as for QFI. For the input state $\rho_P \otimes \rho_A$ indicated by Eqs. (14) and (15), the output state after the two-step evolution reads

$$\begin{aligned} \rho(\theta) &= U_\theta \rho_P \otimes \rho_A U_\theta^\dagger \\ &= \sum_{m,m'=-j}^j \sum_{i=1}^d \frac{p_i p_{i,m,m'}}{2} |j, m\rangle_{\text{opt}}\langle j, m'| \\ &\otimes (e^{i\theta m}|e\rangle + e^{-i\theta m}|g\rangle) \left(e^{-i\theta m'}\langle e| + e^{i\theta m'}\langle g| \right), \end{aligned} \quad (24)$$

where p_i 's are the eigenvalues for the eigenstates $|\psi_i\rangle$ of ρ_P and $p_{i,m,m'} \equiv \langle j, m|\psi_i\rangle\langle\psi_i|j, m'\rangle_{\text{opt}}$. Subsequently, we perform the projective measurements $\{|\Psi_{m,\pm}\rangle\langle\Psi_{m,\pm}|\}$ on the full system as described in Fig. 1, where $|\Psi_{m,\pm}\rangle = |j, m\rangle_{\text{opt}} \otimes |\pm\rangle$ with $|\pm\rangle = (|e\rangle \pm |g\rangle)/\sqrt{2}$, the eigenstates of σ_x for the ancillary qubit. Note $|j, m\rangle_{\text{opt}}$'s are eigenstates of $J(\pi/2 - \phi_{\text{opt}})$ determined by g , ω_P , and ω_A in advance. The probability about detecting the output state in the basis $|\Psi_{m,\pm}\rangle$ reads

$$\begin{aligned} P(m, \pm|\theta) &= \langle\Psi_{m,\pm}|\rho(\theta)|\Psi_{m,\pm}\rangle \\ &= \frac{1}{4} \sum_{i=1}^d p_i p_{i,m,m} |e^{i\theta m} \pm e^{-i\theta m}|^2 \\ &= \frac{1 \pm \cos(2m\theta)}{2} \sum_{i=1}^d p_i p_{i,m,m}. \end{aligned} \quad (25)$$

By the probability distribution $P(m, \pm|\theta)$ [67–69], CFI can be calculated as

$$F_c = \sum_{m=-j}^j \left\{ \frac{[dP(m, +|\theta)/d\theta]^2}{P(m, +|\theta)} + \frac{[dP(m, -|\theta)/d\theta]^2}{P(m, -|\theta)} \right\}. \quad (26)$$

The first derivative of $P(m, \pm|\theta)$ with respect to the to-be-estimated phase θ is $dP(m, \pm|\theta)/d\theta = \mp m \sin(2m\theta) \sum_{i=1}^d p_i p_{i,m,m}$ and hence

$$\frac{[dP(m, \pm|\theta)/d\theta]^2}{P(m, \pm|\theta)} = \frac{2m^2 \sin^2(2m\theta)}{1 \pm \cos(2m\theta)} \sum_{i=1}^d p_i p_{i,m,m}. \quad (27)$$

Inserting Eq. (27) to Eq. (26), we have

$$\begin{aligned} F_c &= \sum_{m=-j}^j 2m^2 \left(\sum_{i=1}^d p_i p_{i,m,m} \right) \sin^2(2m\theta) \\ &\quad \times \left[\frac{1}{1 + \cos(2m\theta)} + \frac{1}{1 - \cos(2m\theta)} \right] \\ &= 4 \sum_{m=-j}^j \sum_{i=1}^d m^2 p_i p_{i,m,m} \\ &= 4 \sum_{i=1}^d p_i \langle \psi_i | \left(\sum_{m=-j}^j m^2 |j, m\rangle_{\text{opt}} \langle j, m| \right) | \psi_i \rangle \\ &= 4 \sum_{i=1}^d p_i \langle \psi_i | J \left(\frac{\pi}{2} - \phi_{\text{opt}} \right)^2 | \psi_i \rangle = F_Q. \end{aligned} \quad (28)$$

The last line is exactly the same as Eq. (20) under the optimized condition in Eq. (18), independent of ρ_P . It is thus verified that QFI can attain its upper-bound in our qubit-assisted metrology. In addition, when the probe is prepared as a polarized state $\rho_P^{\text{opt}} = |j, \pm j\rangle_{\text{opt}} \langle j, \pm j|$, Eq. (25) reduces to

$$P(m, \pm|\theta) = \delta_{m,j} \frac{1 \pm \cos(2m\theta)}{2}, \quad (29)$$

which implies that the magnitude of θ can be inferred from the probability $P(j, +|\theta)$ and $P(j, -|\theta)$. In this case, only performing the projective measurement on the ancillary qubit ρ_A yields the Heisenberg-scaling limit $F_c = F_Q = N^2$.

The result about the polarized probe spin ensemble could be confirmed by the numerical simulation of CFI in Fig. 4, where the initial state of the ancillary qubit is optimized with $\theta_0 = \pi/2$ and the frequencies of the two components are the same as in Fig. 3. The dynamics of the output state $\rho(\theta)$ with a general t_2 can be obtained by the unitary operator in Eq. (2) and that under time-reversal strategy is obtained by Eq. (24). And hence F_c can be numerically evaluated by performing the projective measurements $\{|\pm\rangle\langle\pm|\}$ on the ancillary qubit. In Fig. 4(a), we plot the renormalized CFI F_c/N^2 in space of t_1 and t_2 , when the probe spin number is chosen as an odd number $N = 5$. It is found that the regions around $gt_1 = \pi/2$ [that is in agreement with Eq. (18) with $n = 0$] describes the optimized condition for the Heisenberg-scaling metrology. And it can be more clearly described by the blue solid line in Fig. 4(b), when we fix $gt_1 = \pi/2$. Moreover, the red dashed line indicates the maximum value of CFI with gt_1 running from 0 to π . One

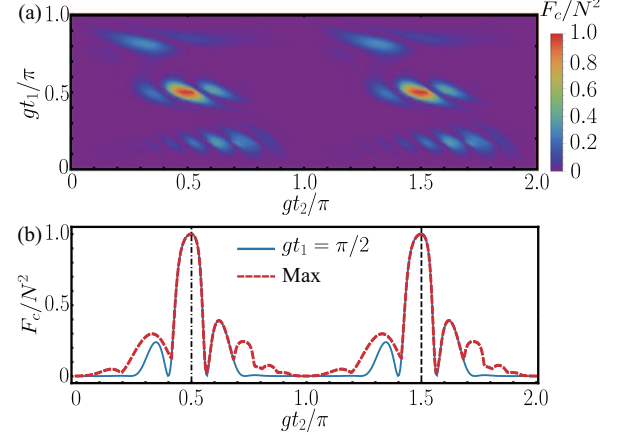


FIG. 4. (a) Renormalized CFI F_c/N^2 in space of gt_1 and gt_2 . (b) Renormalized CFI F_c/N^2 as a function of gt_2 with a fixed $gt_1 = \pi/2$ (blue solid line) and its maximum value obtained with a varying gt_1 (red dashed line). The vertical black dashed line represents the analytical result in Eq. (9). The probe spin ensemble and the ancillary qubit are initialized in the state $\rho_P^{\text{opt}} = |j, j\rangle_{\text{opt}} \langle j, j|$ and $|\varphi\rangle = (|e\rangle + |g\rangle)/\sqrt{2}$, respectively. The other parameters are $\phi_{\text{opt}} = \omega_P \pi/(2g)$, $N = 5$, and $\omega_P = \omega_A = 3g$.

can find that they periodically match with each other. Note the second maximum point in the plot $t_2 = 3\pi/(2g)$ (see the vertical black dashed line) can be predicted by Eq. (9).

It is interesting to find that CFI also attains the Heisenberg scaling $F_c = N^2$ when $t_2 = \pi/(2g)$ [see the vertical black dot-dashed line in Fig. 4(b)]. It is beyond the sufficient condition for the time-reversal strategy as illustrated by Eq. (9) and Fig. 2. However, it is straightforward to see that when $t_1 = t_2 = \pi/(2g)$, the full time-evolution operator in the end can be written as $U'_\theta = U(\pi/g)U^\dagger(t_1)R_x(\theta)U(t_1) = \sigma_z U_\theta$, where U_θ is given by Eq. (13). Then using Eq. (24), we have $\rho'(\theta) = \sigma_z U_\theta \rho_P \otimes \rho_A U_\theta^\dagger \sigma_z = \sigma_z \rho(\theta) \sigma_z$ and hence the probability distribution in Eq. (29) becomes $P'(j, \pm|\theta) = [1 \mp \cos(2m\theta)]/2$, which means $P'(j, \pm|\theta) = P(j, \mp|\theta)$. It indicates that one can still extract all the information encoded in the probe state from the output probabilities and thus $F_c = N^2$.

VI. DISCUSSION

Quantum metrology is conventionally regarded as a parametric-estimation protocol using entanglement or quadratical squeezing to improve the estimation precision beyond the standard quantum limit with respect to the system size N . A benchmark result is that the photonic entangled NOON states are capable to attain the Heisenberg scaling characterized with an N^2 -dependent quantum Fisher information. However, a feasible implementation is limited to the number of photons or exci-

tations due to the difficulty in generating a large-scale and high-fidelity NOON state [29–32], which achieves up to $N = 5$ so far in experiment [31]. As for the spin squeezing that is generated in the nonlinear atom-atom interaction platform, the OAT squeezing demonstrates a scaling below the Heisenberg-limited measurement precision with $\propto 1/N^{2/3}$, e.g., in the cold thermal ensembles [45], the metrological gain is then found to be up to $(\delta\theta_{\text{SQL}}/\delta\theta)^2 \sim 100$ with 10^6 atoms.

In contrast, our qubit-assisted metrology protocol can be enhance QFI up to the Heisenberg scaling of N^2 with respect to the total probe-spin number N , even when the probe system is in a mixed state. More than the ZZ interaction between the ancillary qubit and the probe large-spin in the full Hamiltonian (1), our protocol is applicable to another spin-spin-bath model [70–73] with Hamiltonian

$$H = H_0 + H_I = \omega_P J_z + \omega_A \sigma_z + g J_x \sigma_z. \quad (30)$$

The corresponding circuit model for the qubit-assisted metrology in Fig. 1 is almost invariant, except that the encoded phase parameter θ is now obtained by another rotation $R_z(\theta) = \exp(-i\theta J_z)$ of the probe system. Thus the circuit is described by

$$U_\theta = U(t_2)R_z(\theta)U(t_1) = e^{-iHt_2}e^{-i\theta J_z}e^{-iHt_1}. \quad (31)$$

Using the modified full Hamiltonian (30), Eq. (5) becomes

$$\begin{aligned} U(t_1 + t_2) = U(T) &= \sum_{m=-j}^j \tilde{C}_{e,m} |j, m\rangle_\phi \langle j, m| \otimes |e\rangle \langle e| \\ &+ \sum_{m'=-j}^j \tilde{C}_{g,m'} |j, m'\rangle_{\phi'} \langle j, m'| \otimes |g\rangle \langle g|, \end{aligned} \quad (32)$$

where $\tilde{C}_{e/g,m} = \exp[-i(m\tilde{\omega} \pm \omega_A)T]$ with $\tilde{\omega} \equiv \sqrt{\omega_P^2 + g^2}$. Here $|j, m\rangle_\phi$ and $|j, m'\rangle_{\phi'}$ with eigenvalues m and m' denote the eigenstates of the operators $(\omega_P J_z + g J_x)/\tilde{\omega}$ and $(\omega_P J_z - g J_x)/\tilde{\omega}$, respectively. According to U_θ in Eq. (31) and the time-reversal condition in Eq. (3), we have

$$\begin{aligned} U_{\theta=0} &= e^{-iH(t_1+t_2)} = U(t_1 + t_2) = \mathcal{I}^{2(N+1)} \\ &= \sum_{m=-j}^j |j, m\rangle_\phi \langle j, m| \otimes |e\rangle \langle e| \\ &+ \sum_{m'=-j}^j |j, m'\rangle_{\phi'} \langle j, m'| \otimes |g\rangle \langle g|. \end{aligned} \quad (33)$$

Equation (32) becomes equivalent to Eq. (33) up to a global phase when

$$\tilde{C}_{e,m} = \tilde{C}_{g,m'}. \quad (34)$$

A sufficient solution for Eq. (34) is found to be independent of the parity of the probe-spin number N , and reads,

$$\frac{\tilde{\omega}T}{\pi} = 2n_5, \quad \frac{\omega_A T}{\pi} = n_6, \quad (35)$$

where n_j 's, $j = 5, 6$, are proper integers.

With a proper T on the time-reversal strategy, the whole unitary evolution operator in Eq. (31) can be rewritten as

$$U_\theta = e^{iHt_1} e^{-i\theta J_z} e^{-iHt_1}. \quad (36)$$

Using the Baker-Campbell-Hausdorff formula, we have

$$U_\theta = e^{i\theta(c_z J_z + c_x J_x \sigma_z + c_y J_y \sigma_z)}, \quad (37)$$

where the coefficients of the phase generator are

$$\begin{aligned} c_z &= -\frac{g^2}{\tilde{\omega}^2} \cos(\tilde{\omega}t_1) - \frac{\omega_P^2}{\tilde{\omega}^2}, \\ c_x &= \frac{g\omega_P}{\tilde{\omega}^2} [\cos(\tilde{\omega}t_1) - 1], \\ c_y &= -\frac{g}{\tilde{\omega}} \sin(\tilde{\omega}t_1). \end{aligned} \quad (38)$$

We are now on the stage of minimizing the magnitude of the second term in Eq. (16) to enhance QFI. With Eqs. (37), (14), and (15), we have

$$\begin{aligned} &\langle \psi_i | \langle \varphi | U_\theta^\dagger (\partial_\theta U_\theta) | \varphi \rangle | \psi_i \rangle \\ &= c_z \langle J_z \rangle_{\psi_i} + \langle \sigma_z \rangle_\varphi \langle c_x J_x + c_y J_y \rangle_{\psi_i}. \end{aligned} \quad (39)$$

Under a proper state of the ancillary qubit and an optimized evolution time for Step 1, i.e.,

$$\theta_0 = \frac{\pi}{2}, \quad t_1 = \tilde{\omega}^{-1} \left[\arccos \left(-\frac{\omega_P^2}{g^2} \right) + 2n\pi \right], \quad (40)$$

with an integer n , both terms in Eq. (39) can vanish at the same time for arbitrary probe state ψ_i .

Using Eqs. (16) and (40), QFI becomes the mean square of a phase generator, i.e.,

$$F_Q = 4 \sum_{i=1}^d p_i \langle (c_x J_x + c_y J_y)^2 \rangle_{\psi_i}. \quad (41)$$

It reaches the maximum value $F_Q = N^2$ when the probe spin ensemble is a pure state $|j, j\rangle'_{\text{opt}}$, or $|j, -j\rangle'_{\text{opt}}$, and or a mixed state over them. Here $|j, m\rangle'_{\text{opt}}$ with $-j \leq m \leq j$ denotes the eigenstate for the optimized collective angular momentum operator $c_x J_x + c_y J_y$.

It is evident to see that QFIs in Eqs. (20) and (41) are in the same formation, although with distinct optimized collective angular momentum operator determined by the corresponding interaction Hamiltonian between probe and ancillary qubit. Then following the same optimized procedure from the output state (24) through the first derivative of the probability distribution for the detection (27), one can verify that QFI can attain its upper-bound in our qubit-assisted metrology, i.e., $F_c = F_Q$, only by replacing $|j, m\rangle_{\text{opt}}$ with $|j, m\rangle'_{\text{opt}}$. Again, when the probe is prepared as a polarized state $|j, \pm j\rangle'_{\text{opt}} \langle j, \pm j|$, the Heisenberg-scaling limit $F_c = F_Q = N^2$ can be attained only by performing the projective measurement $|\pm\rangle \langle \pm|$ on the ancillary qubit.

Since $\arccos(x)$ ranges from -1 to 1 , the optimal evolution time t_1 in Eq. (40) can only be obtained in the deep strong coupling regime $g \geq \omega_P$. When $g < \omega_P$, only the second term in Eq. (39) can vanish for arbitrary probe state and the minimum magnitude of the first term associated with c_z can be found at $\cos(\tilde{\omega}t_1) = -1$. The optimal condition, that does not render $F_Q = N^2$, can thus be rewritten as

$$\theta_0 = \frac{\pi}{2}, \quad t_1 = \frac{(2n+1)\pi}{\tilde{\omega}}, \quad (42)$$

with an integer n .

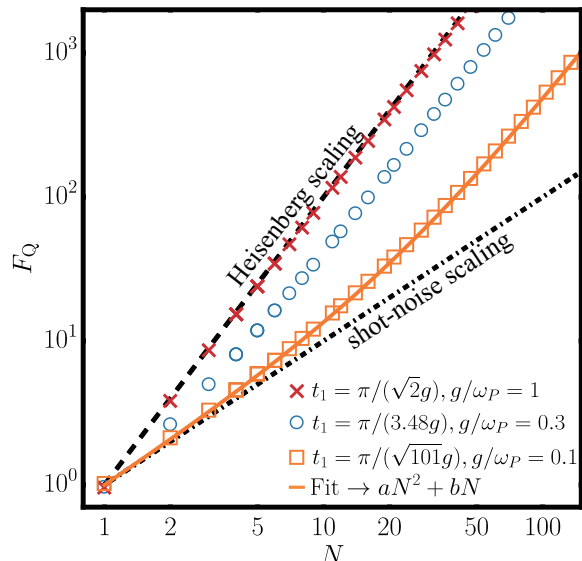


FIG. 5. QFI as a function of N for $t_1 = \pi/(\sqrt{2}g)$ and $g/\omega_P = 1$ (red crosses); for $t_1 = \pi/(3.48g)$ and $g/\omega_P = 0.3$ (blue circles); for $t_1 = \pi/(\sqrt{101}g)$ and $g/\omega_P = 0.1$ (orange squares). The orange solid line is a fit curve for the last case with $F_Q = aN^2 + bN$, where $a \approx 0.04$ and $b \approx 0.96$. The black dashed line and the black dot-dashed lines indicate the Heisenberg scaling N^2 and the shot-noise scaling N .

In Fig. 5, we show the dependence of QFI on the probe-spin number N under various t_1 and g/ω_P according to Eq. (40) or Eq. (42) with $n = 0$, where the initial state of the probe ensemble is set as $\rho_P^{\text{opt}} = |j, j\rangle_{\text{opt}}' \langle j, j|$. Numerical simulation confirms that when $g = \omega_P$, QFI attains its peak value $F_Q = N^2$. The scaling behavior of QFI gradually deviates from the Heisenberg limit with a decreasing g . Yet the numerical fitting for $g/\omega_P = 0.1$ (see the orange solid line and the orange squares) indicate that QFI will follow the Heisenberg scaling in an asymptotic way. It is found that $F_Q \approx 0.04N^2 + 0.96N$, where the two coefficients are dependent on g/ω_P yet independent of N .

VII. CONCLUSION

In summary, we incorporate the joint-evolution-and-quantum-measurement idea to quantum parameter estimation in our metrology protocol. With no input of entangled or squeezed state and with no use of nonlinear Hamiltonian, QFI about the phase encoded into the probe system can be optimized to be the mean square of an optimized phase generator with respect to the probe initial state. That renders an exact or asymptotic Heisenberg-scaling behavior in terms of the spin number N even when the probe starts from a thermal state. And the numerical simulation shows that the imperfections in preparing the ancillary qubit and optimizing the evolution time does not change the Heisenberg-scaling behavior about metrology precision as long as N is sufficiently large. By virtue of the time-reversal strategy and the projective measurement on the whole system or merely the ancillary qubit, CFI is found to be saturated with its quantum counterpart. Our protocol of qubit-assisted quantum metrology is applicable to a general spin-spin-bath model. It therefore provides an economical way toward the Heisenberg-scaling metrology.

ACKNOWLEDGMENTS

We acknowledge financial support from the National Natural Science Foundation of China (Grant No. 11974311).

Appendix A: Evolution operator for time-reversal strategy in the qubit-assisted metrology

This appendix derives the unitary evolution operator for the time-reversal strategy in our qubit-assisted metrology. With the time-reversal condition (3), the whole evolution operator in Eq. (12) can be written as

$$\begin{aligned} U_\theta &= e^{iHt_1} e^{-i\theta J_x} e^{-iHt_1} \\ &= e^{iHt_1} \left[\sum_{k=0}^{\infty} \frac{1}{k!} (-i\theta J_x)^k \right] e^{-iHt_1} \\ &= \sum_{k=0}^{\infty} \frac{1}{k!} (-i\theta e^{iHt_1} J_x e^{-iHt_1})^k \\ &= \exp(-i\theta e^{iHt_1} J_x e^{-iHt_1}). \end{aligned} \quad (A1)$$

Using the full Hamiltonian (1) and the commutation relation $[J_z, \sigma_z] = 0$,

$$\begin{aligned} &e^{iHt_1} J_x e^{-iHt_1} \\ &= e^{igt_1 J_z \sigma_z} (e^{i\omega_P t_1 J_z} J_x e^{-i\omega_P t_1 J_z}) e^{-igt_1 J_z \sigma_z} \\ &= \cos(\omega_P t_1) e^{igt_1 J_z \sigma_z} J_x e^{-igt_1 J_z \sigma_z} \\ &\quad - \sin(\omega_P t_1) e^{igt_1 J_z \sigma_z} J_y e^{-igt_1 J_z \sigma_z}. \end{aligned} \quad (A2)$$

In the last step, we have used $e^{i\alpha J_z} J_x e^{-i\alpha J_z} = \cos(\alpha) J_x - \sin(\alpha) J_y$. The Baker-Campbell-Hausdorff formula yields:

$$e^{igt_1 J_z \sigma_z} J_x e^{-igt_1 J_z \sigma_z} = \sum_{k=0}^{\infty} \frac{1}{k!} C_k, \quad (\text{A3})$$

where $C_{k+1} = igt_1[J_z \sigma_z, C_k]$ and $C_0 = J_x$. Using the commutation relation $[J_\alpha, J_\beta] = i\epsilon_{\alpha\beta\gamma} J_\gamma$ with $\epsilon_{\alpha\beta\gamma}$ the Levi-Civita tensor, we have

$$\begin{aligned} C_1 &= igt_1[J_z \sigma_z, C_0] = -gt_1 J_y \sigma_z, \\ C_2 &= igt_1[J_z \sigma_z, C_1] = -(gt_1)^2 J_x, \\ C_3 &= igt_1[J_z \sigma_z, C_2] = (gt_1)^3 J_y \sigma_z, \end{aligned} \quad (\text{A4})$$

and so on. Equation (A3) thus becomes

$$\begin{aligned} &e^{igt_1 J_z \sigma_z} J_x e^{-igt_1 J_z \sigma_z} \\ &= J_x \sum_{k=0}^{\infty} \frac{(-1)^k}{(2k)!} (gt_1)^{2k} - J_y \sigma_z \sum_{k=0}^{\infty} \frac{(-1)^k}{(2k+1)!} (gt_1)^{2k+1} \\ &= \cos(gt_1) J_x - \sin(gt_1) J_y \sigma_z. \end{aligned} \quad (\text{A5})$$

And similarly, we have

$$e^{igt_1 J_z \sigma_z} J_y e^{-igt_1 J_z \sigma_z} = \cos(gt_1) J_y + \sin(gt_1) J_x \sigma_z. \quad (\text{A6})$$

Therefore, Eq. (A2) can be reduced to

$$\begin{aligned} &e^{iHt_1} J_x e^{-iHt_1} \\ &= \cos(gt_1) [\cos(\omega_P t_1) J_x - \sin(\omega_P t_1) J_y] \\ &\quad - \sin(gt_1) [\cos(\omega_P t_1) J_y + \sin(\omega_P t_1) J_x] \sigma_z, \end{aligned} \quad (\text{A7})$$

and hence

$$U_\theta = e^{-i\theta [\cos(gt_1) J(-\phi) - \sin(gt_1) J(\frac{\pi}{2} - \phi) \sigma_z]}, \quad (\text{A8})$$

where $J(\phi) \equiv \cos(\phi) J_x + \sin(\phi) J_y$ and $\phi = \omega_P t_1$. It is exactly Eq. (13) in the main text.

[1] Z. Sun, J. Ma, X.-M. Lu, and X. Wang, *Fisher information in a quantum-critical environment*, *Phys. Rev. A* **82**, 022306 (2010).

[2] J. Ma, Y.-x. Huang, X. Wang, and C. P. Sun, *Quantum fisher information of the greenberger-horne-zeilinger state in decoherence channels*, *Phys. Rev. A* **84**, 022302 (2011).

[3] M. G. Genoni, S. Olivares, D. Brivio, S. Cialdi, D. Cipriani, A. Santamato, S. Vezzoli, and M. G. A. Paris, *Optical interferometry in the presence of large phase diffusion*, *Phys. Rev. A* **85**, 043817 (2012).

[4] B. M. Escher, L. Davidovich, N. Zagury, and R. L. de Matos Filho, *Quantum metrological limits via a variational approach*, *Phys. Rev. Lett.* **109**, 190404 (2012).

[5] W. Zhong, Z. Sun, J. Ma, X. Wang, and F. Nori, *Fisher information under decoherence in bloch representation*, *Phys. Rev. A* **87**, 022337 (2013).

[6] M. G. Paris, *Quantum estimation for quantum technology*, *Int. J. Quantum Inf.* **7**, 125 (2009).

[7] C. W. Helstrom, *Quantum detection and estimation theory*, *J. Stat. Phys.* **1**, 231 (1969).

[8] B. Yurke, S. L. McCall, and J. R. Klauder, *Su(2) and su(1,1) interferometers*, *Phys. Rev. A* **33**, 4033 (1986).

[9] C. M. Caves, *Quantum-mechanical noise in an interferometer*, *Phys. Rev. D* **23**, 1693 (1981).

[10] M. A. Taylor and W. P. Bowen, *Quantum metrology and its application in biology*, *Phys. Rep.* **615**, 1 (2016).

[11] N. Mauranyapin, L. Madsen, M. Taylor, M. Waleed, and W. Bowen, *Evanescent single-molecule biosensing with quantum-limited precision*, *Nat. Photonics* **11**, 477 (2017).

[12] A. D. Ludlow, M. M. Boyd, J. Ye, E. Peik, and P. O. Schmidt, *Optical atomic clocks*, *Rev. Mod. Phys.* **87**, 637 (2015).

[13] H. Katori, *Optical lattice clocks and quantum metrology*, *Nat. Photonics* **5**, 203 (2011).

[14] J. A. Jones, S. D. Karlen, J. Fitzsimons, A. Ardavan, S. C. Benjamin, G. A. D. Briggs, and J. J. Morton, *Magnetic field sensing beyond the standard quantum limit using 10-spin noon states*, *Science* **324**, 1166 (2009).

[15] V. Giovannetti, S. Lloyd, and L. Maccone, *Advances in quantum metrology*, *Nat. Photonics* **5**, 222 (2011).

[16] G. Tóth and I. Apellaniz, *Quantum metrology from a quantum information science perspective*, *J. Phys. A: Math. Theor.* **47**, 424006 (2014).

[17] W. Nawrocki, *Introduction to quantum metrology*, 2nd ed. (Springer Nature Switzerland, Cham, Switzerland, 2019).

[18] E. Polino, M. Valeri, N. Spagnolo, and F. Sciarrino, *Photonic quantum metrology*, *AVS Quantum Sci.* **2**, 024703 (2020).

[19] A. S. Holevo, *Probabilistic and statistical aspects of quantum theory* (North-Holland, Amsterdam, 1982).

[20] S. L. Braunstein and C. M. Caves, *Statistical distance and the geometry of quantum states*, *Phys. Rev. Lett.* **72**, 3439 (1994).

[21] S. L. Braunstein, C. M. Caves, and G. J. Milburn, *Generalized uncertainty relations: theory, examples, and lorentz invariance*, *Ann. Phys.* **247**, 135 (1996).

[22] S. Luo, *Wigner-yanase skew information and uncertainty relations*, *Phys. Rev. Lett.* **91**, 180403 (2003).

[23] L. Pezzé and A. Smerzi, *Entanglement, nonlinear dynamics, and the heisenberg limit*, *Phys. Rev. Lett.* **102**, 100401 (2009).

[24] M. Kacprowicz, R. Demkowicz-Dobrzański, W. Wasilewski, K. Banaszek, and I. Walmsley, *Experimental quantum-enhanced estimation of a lossy phase shift*, *Nat. Photonics* **4**, 357 (2010).

[25] D. Leibfried, M. D. Barrett, T. Schaetz, J. Britton, J. Chiaverini, W. M. Itano, J. D. Jost, C. Langer, and D. J. Wineland, *Toward heisenberg-limited spectroscopy with multiparticle entangled states*, *Science* **304**, 1476 (2004).

[26] M. W. Mitchell, J. S. Lundeen, and A. M. Steinberg, *Super-resolving phase measurements with a multiphoton entangled state*, *Nature* **429**, 161 (2004).

[27] A. N. Boto, P. Kok, D. S. Abrams, S. L. Braunstein, C. P. Williams, and J. P. Dowling, *Quantum interferometric optical lithography: Exploiting entanglement to beat the diffraction limit*, *Phys. Rev. Lett.* **85**, 2733 (2000).

[28] C. C. Gerry, *Heisenberg-limit interferometry with four-wave mixers operating in a nonlinear regime*, *Phys. Rev. A* **61**, 043811 (2000).

[29] J. J. Bollinger, W. M. Itano, D. J. Wineland, and D. J. Heinzen, *Optimal frequency measurements with maximally correlated states*, *Phys. Rev. A* **54**, R4649 (1996).

[30] P. Walther, J.-W. Pan, M. Aspelmeyer, R. Ursin, S. Gasparoni, and A. Zeilinger, *De broglie wavelength of a non-local four-photon state*, *Nature* **429**, 158 (2004).

[31] I. Afek, O. Ambar, and Y. Silberberg, *High-noon states by mixing quantum and classical light*, *Science* **328**, 879 (2010).

[32] Y. M. Zhang, X. W. Li, W. Yang, and G. R. Jin, *Quantum fisher information of entangled coherent states in the presence of photon loss*, *Phys. Rev. A* **88**, 043832 (2013).

[33] D. J. Wineland, J. J. Bollinger, W. M. Itano, F. L. Moore, and D. J. Heinzen, *Spin squeezing and reduced quantum noise in spectroscopy*, *Phys. Rev. A* **46**, R6797 (1992).

[34] M. Kitagawa and M. Ueda, *Squeezed spin states*, *Phys. Rev. A* **47**, 5138 (1993).

[35] D. J. Wineland, J. J. Bollinger, W. M. Itano, and D. J. Heinzen, *Squeezed atomic states and projection noise in spectroscopy*, *Phys. Rev. A* **50**, 67 (1994).

[36] K. Goda, O. Miyakawa, E. E. Mikhailov, S. Saraf, R. Adhikari, K. McKenzie, R. Ward, S. Vass, A. J. Weinstein, and N. Mavalvala, *A quantum-enhanced prototype gravitational-wave detector*, *Nat. Phys.* **4**, 472 (2008).

[37] Y. C. Liu, Z. F. Xu, G. R. Jin, and L. You, *Spin squeezing: Transforming one-axis twisting into two-axis twisting*, *Phys. Rev. Lett.* **107**, 013601 (2011).

[38] Y.-C. Zhang, X.-F. Zhou, X. Zhou, G.-C. Guo, and Z.-W. Zhou, *Cavity-assisted single-mode and two-mode spin-squeezed states via phase-locked atom-photon coupling*, *Phys. Rev. Lett.* **118**, 083604 (2017).

[39] C. Gross, T. Zibold, E. Nicklas, J. Esteve, and M. K. Oberthaler, *Nonlinear atom interferometer surpasses classical precision limit*, *Nature* **464**, 1165 (2010).

[40] M. F. Riedel, P. Böhi, Y. Li, T. W. Hänsch, A. Sinatra, and P. Treutlein, *Atom-chip-based generation of entanglement for quantum metrology*, *Nature* **464**, 1170 (2010).

[41] J. G. Bohnet, B. C. Sawyer, J. W. Britton, M. L. Wall, A. M. Rey, M. Foss-Feig, and J. J. Bollinger, *Quantum spin dynamics and entanglement generation with hundreds of trapped ions*, *Science* **352**, 1297 (2016).

[42] Y. Lu, S. Zhang, K. Zhang, W. Chen, Y. Shen, J. Zhang, J.-N. Zhang, and K. Kim, *Global entangling gates on arbitrary ion qubits*, *Nature* **572**, 363 (2019).

[43] C. Song, K. Xu, H. Li, Y.-R. Zhang, X. Zhang, W. Liu, Q. Guo, Z. Wang, W. Ren, J. Hao, *et al.*, *Generation of multicomponent atomic schrödinger cat states of up to 20 qubits*, *Science* **365**, 574 (2019).

[44] K. Xu, Z.-H. Sun, W. Liu, Y.-R. Zhang, H. Li, H. Dong, W. Ren, P. Zhang, F. Nori, D. Zheng, *et al.*, *Probing dynamical phase transitions with a superconducting quantum simulator*, *Sci. Adv.* **6**, eaba4935 (2020).

[45] O. Hosten, N. J. Engelsen, R. Krishnakumar, and M. A. Kasevich, *Measurement noise 100 times lower than the quantum-projection limit using entangled atoms*, *Nature* **529**, 505 (2016).

[46] H. Bao, J. Duan, S. Jin, X. Lu, P. Li, W. Qu, M. Wang, I. Novikova, E. E. Mikhailov, K.-F. Zhao, *et al.*, *Spin squeezing of 1011 atoms by prediction and retrodiction measurements*, *Nature* **581**, 159 (2020).

[47] J. Duan, Z. Hu, X. Lu, L. Xiao, S. Jia, K. Mølmer, and Y. Xiao, *Continuous field tracking with machine learning and steady state spin squeezing*, *arXiv:2402.00536* (2024).

[48] J. Borregaard, E. Davis, G. S. Bentsen, M. H. Schleier-Smith, and A. S. Sørensen, *One-and two-axis squeezing of atomic ensembles in optical cavities*, *New J. Phys.* **19**, 093021 (2017).

[49] K. Helmerson and L. You, *Creating massive entanglement of bose-einstein condensed atoms*, *Phys. Rev. Lett.* **87**, 170402 (2001).

[50] V. Macrì, F. Nori, S. Savasta, and D. Zueco, *Spin squeezing by one-photon–two-atom excitation processes in atomic ensembles*, *Phys. Rev. A* **101**, 053818 (2020).

[51] D. Li, C.-H. Yuan, Z. Ou, and W. Zhang, *The phase sensitivity of an su (1, 1) interferometer with coherent and squeezed-vacuum light*, *New J. Phys.* **16**, 073020 (2014).

[52] D. Li, B. T. Gard, Y. Gao, C.-H. Yuan, W. Zhang, H. Lee, and J. P. Dowling, *Phase sensitivity at the heisenberg limit in an su(1,1) interferometer via parity detection*, *Phys. Rev. A* **94**, 063840 (2016).

[53] J. Jing, C. Liu, Z. Zhou, Z. Ou, and W. Zhang, *Realization of a nonlinear interferometer with parametric amplifiers*, *Appl. Phys. Lett.* **99**, 011110 (2011).

[54] F. Hudelist, J. Kong, C. Liu, J. Jing, Z. Ou, and W. Zhang, *Quantum metrology with parametric amplifier-based photon correlation interferometers*, *Nat. Commun.* **5**, 3049 (2014).

[55] W. Du, J. Kong, G. Bao, P. Yang, J. Jia, S. Ming, C.-H. Yuan, J. F. Chen, Z. Y. Ou, M. W. Mitchell, and W. Zhang, *Su(2)-in-su(1,1) nested interferometer for high sensitivity, loss-tolerant quantum metrology*, *Phys. Rev. Lett.* **128**, 033601 (2022).

[56] A. M. Marino, N. V. Corzo Trejo, and P. D. Lett, *Effect of losses on the performance of an su(1,1) interferometer*, *Phys. Rev. A* **86**, 023844 (2012).

[57] B. Xia, J. Huang, H. Li, Z. Luo, and G. Zeng, *Nanoradian-scale precision in light rotation measurement via indefinite quantum dynamics*, *arXiv:2310.07125* (2024).

[58] G. S. Agarwal and L. Davidovich, *Quantifying quantum-amplified metrology via fisher information*, *Phys. Rev. Res.* **4**, L012014 (2022).

[59] J. Wang, R. L. d. M. Filho, G. S. Agarwal, and L. Davidovich, *Quantum advantage of time-reversed ancilla-based metrology of absorption parameters*, *Phys. Rev. Res.* **6**, 013034 (2024).

[60] D.-W. Luo and T. Yu, *Time-reversal assisted quantum metrology with an optimal control*, *arXiv:2312.14443* (2023).

[61] G. Gillard, E. Clarke, and E. A. Chekhovich, *Harnessing many-body spin environment for long coherent*

ence storage and high-fidelity single-shot qubit readout, *Nat. Commun.* **13**, 4048 (2022).

[62] A. N. Pyrkov and T. Byrnes, *Entanglement generation in quantum networks of bose-einstein condensates*, *New J. Phys.* **15**, 093019 (2013).

[63] V. Meyer, M. A. Rowe, D. Kielpinski, C. A. Sackett, W. M. Itano, C. Monroe, and D. J. Wineland, *Experimental demonstration of entanglement-enhanced rotation angle estimation using trapped ions*, *Phys. Rev. Lett.* **86**, 5870 (2001).

[64] C. F. Ockeloen, R. Schmied, M. F. Riedel, and P. Treutlein, *Quantum metrology with a scanning probe atom interferometer*, *Phys. Rev. Lett.* **111**, 143001 (2013).

[65] G.-R. Jin, Y.-C. Liu, and W.-M. Liu, *Spin squeezing in a generalized one-axis twisting model*, *New J. Phys.* **11**, 073049 (2009).

[66] J. Liu, X.-X. Jing, W. Zhong, and X.-G. Wang, *Quantum fisher information for density matrices with arbitrary ranks*, *Commun. Theor. Phys.* **61**, 45 (2014).

[67] D. Braun, G. Adesso, F. Benatti, R. Floreanini, U. Marzolino, M. W. Mitchell, and S. Pirandola, *Quantum-enhanced measurements without entanglement*, *Rev. Mod. Phys.* **90**, 035006 (2018).

[68] J. Liu, H. Yuan, X.-M. Lu, and X. Wang, *Quantum fisher information matrix and multiparameter estimation*, *J. Phys. A: Math. Theor.* **53**, 023001 (2020).

[69] K. C. Tan, V. Narasimhachar, and B. Regula, *Fisher information universally identifies quantum resources*, *Phys. Rev. Lett.* **127**, 200402 (2021).

[70] A. O. Caldeira, A. H. Castro Neto, and T. Oliveira de Carvalho, *Dissipative quantum systems modeled by a two-level-reservoir coupling*, *Phys. Rev. B* **48**, 13974 (1993).

[71] J. Shao, M.-L. Ge, and H. Cheng, *Decoherence of quantum-nondemolition systems*, *Phys. Rev. E* **53**, 1243 (1996).

[72] J. Xu, J. Jing, and T. Yu, *Entanglement dephasing dynamics driven by a bath of spins*, *J. Phys. A: Math. Theor.* **44**, 185304 (2011).

[73] H. Wang and J. Shao, *Dynamics of a two-level system coupled to a bath of spins*, *J. Chem. Phys.* **137**, 22A504 (2012).